Measuring dynamic structural changes of nanoparticles at the atomic scale using scanning transmission electron microscopy

Measuring Dynamic Structural Changes of Nanoparticles at the Atomic Scale Using Scanning Transmission Electron Microscopy

Annelies De wael,[1,2] Annick De Backer,[1,2] Lewys Jones,[3,4,5]
Aakash Varambhia,[3,†] Peter D. Nellist,[3] and Sandra Van Aert[1,2,*]

[1]*EMAT, University of Antwerp, Groenenborgerlaan 171, 2020 Antwerp, Belgium*
[2]*NANOlab Center of Excellence, University of Antwerp, Belgium*
[3]*Department of Materials, University of Oxford, Parks Road, OX1 3PH Oxford, United Kingdom*
[4]*Advanced Microscopy Laboratory, Centre for Research on Adaptive Nanostructures and Nanodevices (CRANN), Dublin 2, Ireland*
[5]*School of Physics, Trinity College Dublin, The University of Dublin, Dublin 2, Ireland*

We propose a new method to measure atomic scale dynamics of nanoparticles from experimental high-resolution annular dark field scanning transmission electron microscopy images. By using the so-called hidden Markov model, which explicitly models the possibility of structural changes, the number of atoms in each atomic column can be quantified over time. This newly proposed method outperforms the current atom-counting procedure and enables the determination of the probabilities and cross sections for surface diffusion. This method is therefore of great importance for revealing and quantifying the atomic structure when it evolves over time via adatom dynamics, surface diffusion, beam effects, or during *in situ* experiments.

In the field of atomic resolution electron microscopy, quantitative methods are becoming increasingly important for a reliable structure determination of a nanomaterial in three dimensions [1–6]. However, such quantitative analysis tools largely focus on a stationary structure as a result of which the insight into the dynamics is lacking. Since the atomic structure of a nanomaterial can evolve over time via adatom dynamics [7, 8], surface diffusion and reconstruction [9–13], beam effects [14–17], or during *in situ* experiments [18, 19], a quantitative analysis at a single time-point is often insufficient to understand the atomic structure-properties relationship. Different time-resolving techniques, such as dynamic transmission electron microscopy [20, 21], ultrafast electron diffraction [22–27], and ultrafast x-ray imaging [28, 29] have been developed in order to study structural dynamics with very high temporal resolution. Since these techniques sacrifice direct atomic resolution imaging, high-resolution transmission electron microscopy [30], off-axis electron holography [31], or annular dark field (ADF) scanning transmission electron microscopy (STEM) [32, 33] are needed to obtain local structural information at atomic resolution and subsecond temporal resolution. This time resolution is adequate in order to study transient atomic scale phenomena [19, 34–39]. The concomitant advantage for ADF STEM images is that the intensities are peaked at the atomic column positions and depend monotonically on the atomic mass number Z and the thickness of the material enabling us to count the number of atoms in each atomic column. In this Letter, we propose a method for reliable atom counting from a sequence of ADF STEM images allowing us to measure the dynamic structural changes of nanoparticles.

From the ADF STEM images, we can quantify the total intensity of electrons scattered towards the annular detector from each atomic column. These are the so-called scattering cross sections [40, 41], and are a suitable measure for reliable atom counting [42]. In pure-element nanomaterials, the number of atoms in each atomic column can be determined using these scattering cross sections [32, 33, 43–46]. When the atom-counting results are combined with a structural energy minimization [47–49], we can obtain a visualization of the 3D atomic structure from a 2D image without the need for the large electron doses and long acquisition times generally required for electron tomography. In order to quantify atomic scale dynamics, we will use a so-called hidden Markov model. Hidden Markov models were successful in other fields of science for applications such as speech recognition, sequence alignment of protein structures, electrocardiogram characterization and condition-based maintenance of industrial machines [50–54] and have optimal properties for modeling and analyzing time series data. Here, for the first time, we apply hidden Markov models to ADF STEM data.

A hidden Markov model consists of two layers: a "hidden" Markov chain state sequence and an observed sequence. In order to use hidden Markov models for atom counting, we model the number of atoms in each atomic column of the nanoparticle as the hidden states and the scattering cross sections estimated from the ADF STEM images as the observations. Table 1 in the Supplemental Material [55] summarizes the notation used throughout this Letter. The hidden state sequence is represented by a stochastic tensor $\boldsymbol{H} = (\boldsymbol{h}_1, \cdots, \boldsymbol{h}_T)^{\intercal}$ which contains the states $\boldsymbol{h}_t$ at each time t, with T the total number of frames in the time series. In our method, the state $\boldsymbol{h}_t$ is a binary matrix with elements $h_{tg}^{(n)} = 1$, if and only if at time t, the nth atomic column of the nanoparticle contains g atoms. As such, we consider the number of atoms in each atomic column as a separate hidden state, and we can use the so-called factorial hidden Markov model [56],

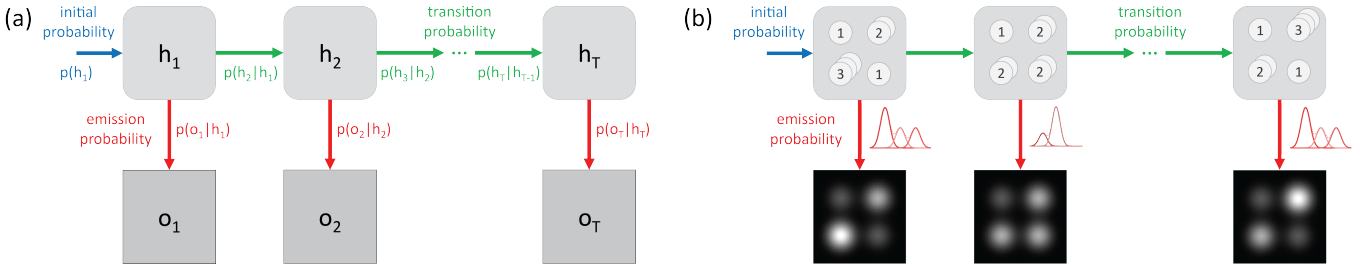

Figure 1. (a) Graphical representation of a hidden Markov model, which consists of a hidden state sequence (top row) and an observed sequence (bottom row), connected through the emission probability (red). The hidden states can have different possible values over time according to initial (blue) and transition probabilities (green). (b) The hidden Markov model for atom counting models the number of atoms in each atomic column of the nanoparticle as the hidden states (top row) and the scattering cross sections obtained from the ADF STEM images as the observations (bottom row).

where the states and model probabilities are factorized over the atomic columns. The observed sequence is represented by the matrix $\boldsymbol{O} = (\boldsymbol{o}_1, \cdots, \boldsymbol{o}_T)^\intercal$, where $\boldsymbol{o}_t$ is the observed vector at time t in the time series, with elements $o_t^{(n)}$, the scattering cross section of the nth atomic column at time t. When $T = 1$, this approach is identical to the existing procedure for atom counting [32, 33, 45, 46]. The (factorial) hidden Markov model is described by the joint probability density function of the hidden state sequence $\boldsymbol{H}$ and the observed sequence $\boldsymbol{O}$:

$$\begin{aligned} &p(\boldsymbol{H}, \boldsymbol{O}; \boldsymbol{\Omega}) \\ &= p\left(\boldsymbol{h}_1; \boldsymbol{I}\right) \prod_{t=2}^{T} p\left(\boldsymbol{h}_t | \boldsymbol{h}_{t-1}; \boldsymbol{A}\right) \prod_{t'=1}^{T} p\left(\boldsymbol{o}_{t'} | \boldsymbol{h}_{t'}; \boldsymbol{\mu}, \sigma\right), \end{aligned} \quad (1)$$

with $\boldsymbol{\Omega} = \{\boldsymbol{I}, \boldsymbol{A}, \boldsymbol{\mu}, \sigma\}$ the parameters of the hidden Markov model. The joint probability density function of Eq. (1) consists of three contributions, schematically shown in Fig. 1. First, the initial probability distribution, defined as follows:

$$p\left(\boldsymbol{h}_1; \boldsymbol{I}\right) = \prod_{n=1}^{N} \prod_{g=0}^{G} \iota_g^{h_{1g}^{(n)}}, \quad (2)$$

with $\boldsymbol{I}$ the vector containing all initial probabilities ι_g for an atomic column to have g atoms in frame 1, G the maximum number of atoms in an atomic column and N the number of atomic columns. Once the state sequence is initialized, the transition probability describes how the states can change from frame to frame in the time series:

$$p\left(\boldsymbol{h}_t | \boldsymbol{h}_{t-1}; \boldsymbol{A}\right) = \prod_{n=1}^{N} \prod_{g_1=0}^{G} \prod_{g_2=0}^{G} A_{g_1 g_2}^{h_{t-1,g_1}^{(n)} h_{t,g_2}^{(n)}}. \quad (3)$$

This is the probability of state $\boldsymbol{h}_t$, given the previous state $\boldsymbol{h}_{t-1}$. The transition probabilities are summarized by the transition matrix $\boldsymbol{A}$, with elements $A_{g_1 g_2}$ the probability that the number of atoms in an atomic column changes from g_1 in one frame to g_2 in the next frame of the time series. The Markov property imposes that the state sequence has no memory: the number of atoms in an atomic column in a frame only depends on the number of atoms in that atomic column in the previous frame, and does not depend on any earlier frames. The hidden Markov model does not impose further restrictions on the physical mechanism causing the changes in the atomic structure. Finally, for each frame, there is an emission probability that describes the probability of an observation, given the hidden state at that time. Ideally, all atomic columns with the same number of atoms result in the same scattering cross section. However, there are fluctuations due to a combination of different effects such as electron counting statistics, instabilities of the microscope, different vertical onset of columns of the same number of atoms, vacancies, relaxation at the boundaries, contamination, intensity transfer between columns, and the influence of neighboring columns of different number of atoms. Therefore, the scattering cross sections are regarded as a statistical draw from a Gaussian distribution, which defines the emission probability:

$$p\left(\boldsymbol{o}_t | \boldsymbol{h}_t; \boldsymbol{\mu}, \sigma\right) = \prod_{n=1}^{N} \prod_{g=0}^{G} \mathcal{N}\left(o_t^{(n)} | \mu_g, \sigma\right)^{h_{tg}^{(n)}}, \quad (4)$$

with $\boldsymbol{\mu}$ the vector containing the average scattering cross sections μ_g for an atomic column with g atoms, and σ the width of the Gaussian distribution, analogous to the approach followed in Refs. [33, 45]. Furthermore, prior knowledge from image simulations is incorporated by imposing a linear scaling between the average scattering cross sections and the scattering cross section resulting from image simulations:

$$\mu_g = a\mathcal{M}_g. \quad (5)$$

In this expression, $\mathcal{M}_g$ is the scattering cross section resulting from image simulations and a is a linear scaling parameter that allows us to compensate for a possible mismatch between experiment and simulation, such as intensity changes due to a slightly different detector inner angle or the intensity loss caused by small sample tilt [46, 57]. This approach was introduced for single

frames as the hybrid method for atom counting, yielding improved atom-counting reliability, especially at low electron doses, compared to alternative approaches [46].

In order to retrieve the hidden state sequence from the observed sequence, the parameters of the factorial hidden Markov model for atom counting are estimated. The unknown parameters are

$$\mathbf{\Omega} = (\iota_0, \cdots, \iota_{G-1}, A_{00}, \cdots, A_{G,G-1}, a, \sigma)\,. \qquad (6)$$

Since $\sum_{g=0}^{G} \iota_g = 1$ and $\sum_{g=0}^{G} A_{jg} = 1 \;\forall\; 0 \leq j \leq G$, $G+2$ parameters (ι_G and A_{jG} with $0 \leq j \leq G$) could be omitted from the parameter vector $\mathbf{\Omega}$. The parameters $\mathbf{\Omega}$ can be estimated using the maximum likelihood estimator [58]. Therefore, the complete data likelihood function of the unknown parameter vector for the observed and hidden data, which follows from Eq. (1), has to be maximized:

$$L(\mathbf{\Omega}; \boldsymbol{H}, \boldsymbol{O}) = p\left(\boldsymbol{h}_1\right) \prod_{t=2}^{T} p\left(\boldsymbol{h}_t | \boldsymbol{h}_{t-1}\right) \prod_{t'=1}^{T} p\left(\boldsymbol{o}_{t'} | \boldsymbol{h}_{t'}\right). \qquad (7)$$

The likelihood can be maximized analytically, by solving the likelihood equation:

$$\frac{\partial \log L(\mathbf{\Omega}; \boldsymbol{H}, \boldsymbol{O})}{\partial \mathbf{\Omega}} = 0. \qquad (8)$$

This equation is solved iteratively, using an expectation-maximization algorithm, usually called the Baum-Welch algorithm in the context of hidden Markov models [50]. Using the estimated parameters, the hidden state sequence with the joint highest probability is retrieved using a path backtracking algorithm, called the Viterbi algorithm [59, 60]. More details about both algorithms are provided in Sec. 1 of the Supplementary Material [55].

In order to illustrate the benefits of this newly developed hidden Markov model for atom counting from a time series, we compare its performance to the hybrid method [46]. For the hybrid method, the scattering cross sections of all frames of the time series are jointly analyzed, such that the counting results are based on the same set of observations as the hidden Markov model. The counting results are then extracted per frame from this so-called collective analysis [61, 62]. We simulated scattering cross sections corresponding to hypothetic ADF STEM time series with 40 frames of a changing Pt nanoparticle with 215 atomic columns, and a thickness up to 15 atoms, similar to the experimental example that will be discussed further in this Letter. The number of atoms in a column can change by ± 1 from frame to frame throughout the time series, with a probability of 10%. An example of the 3D atomic structure of the Pt nanoparticle and how it changes over time is shown in Fig. 2(a). More details about the simulation can be found in Sec. 2 of the Supplementary Material [55]. In Fig. 2(b), the average percentage of correctly counted atomic columns by both methods, with a 95% confidence interval, is evaluated as a function of the electron dose. The hidden Markov model counts the number of atoms in each column more accurately, both at low electron doses, where Poisson noise dominates, and at high electron dose, where the scan distortion is the dominant noise contribution [63]. The improved performance of the hidden Markov model is a direct consequence of using the Viterbi algorithm to retrieve the counting results. The most likely state sequence obtained by this algorithm employs the extra information from the transition probabilities to unravel the states and is therefore not limited strictly by the overlap of the Gaussian distributions around the average scattering cross sections of columns with different thicknesses.

In Figs. 2(c) and 2(d), the underlying transition matrices $\boldsymbol{A}$ are shown for a noise realization at low and high electron dose respectively. In Figs. 2(e)-2(h), we show the estimated transition matrices using both methods for the respective low and high dose noise realizations. The transition matrix for the collective hybrid method was estimated by considering the obtained atom-counting results as a Markov chain. The transition matrix summarizes the estimated structural changes of the nanoparticle: diagonal elements correspond to the probabilities that the number of atoms in an atomic column with a given thickness does not change from one frame to the next and off-diagonal elements in the lower and upper triangle correspond to the probabilities for an atomic column to lose or gain atoms respectively. From the comparison of Figs. 2(g) and 2(h) with the respective ground truth in Figs. 2(c) and 2(d), it is clear that the collective hybrid method overinterprets intensity variations during the time series as actual thickness changes, both at low and high electron doses. From Figs. 2(e) and 2(f) on the other hand, it is clear that the hidden Markov model far more accurately retrieves the transition probabilities, and therefore opens up possibilities for a reliable quantification of dynamic structural changes of nanoparticles at the atomic scale.

Next, we apply this to an experimental time series of a catalyst Pt nanoparticle. ADF STEM images were recorded on a JEOL ARM200CF fitted with a probe-aberration corrector using an acceleration voltage of 200 kV, a probe convergence angle of 22.48 mrad, an annular detector ranging from 52-248 mrad, a dwell time of 4μs and an electron dose of 1.38×10^4 e$^-$/Å^2 per frame. All images of the time series are shown in Fig. S1 of the Supplemental Material [55]. The images from the time series were corrected for drift and other distortions using nonrigid registration [64]. Coordinates of the atomic columns were selected in each frame using the maximum *a posteriori* probability (MAP) rule for atomic column detection introduced in [65]. As such, we could reliably determine all atomic columns present in the nanoparticle throughout the time series. During the time series, the Pt nanoparticle tilts slightly away from zone axis orienta-

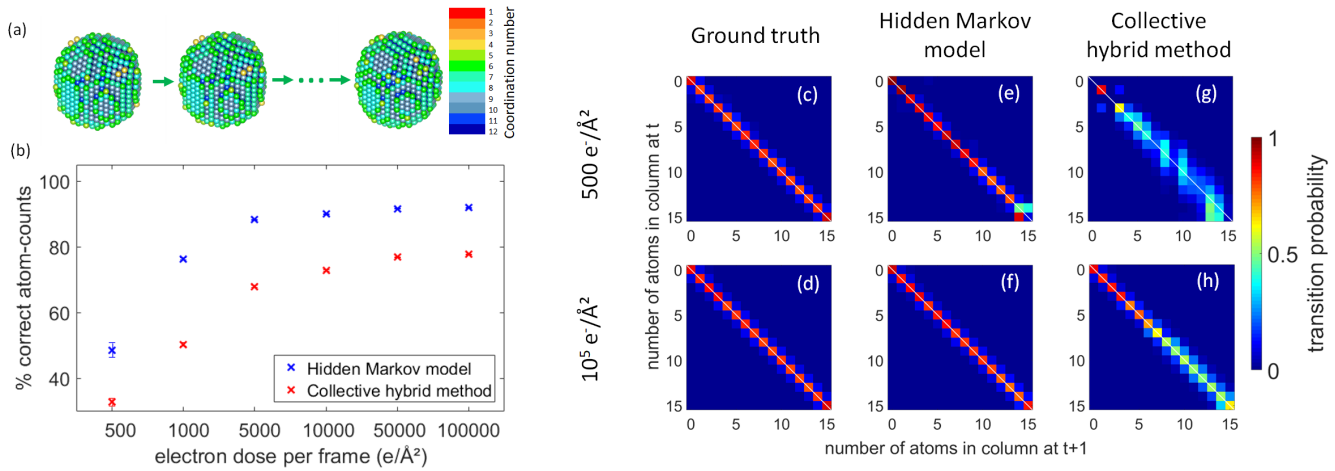

Figure 2. (a) Example of the 3D atomic structure of the changing Pt nanoparticle. (b) Percentage of correctly counted atomic columns, with a 95% confidence interval as a function of the electron dose in each individual frame. (c)-(h) Ground truth and estimated transition matrices using the hidden Markov model analysis and the collective hybrid method with electron dose 5×10^2 and 10^5 $e^-/Å^2$.

tion and back, which affects the scattering cross sections [57]. However, the hidden Markov model only estimates one linear scaling parameter for all frames of the time series. Therefore, the scattering cross sections of the individual frames need to be compensated for tilt, prior to the hidden Markov model analysis. This is done by using a linear scaling of the scattering cross sections of the individual frames [46], assuming that the total number of atoms in the nanoparticle remains constant throughout the time series. This assumption is valid since the threshold energy for sputtering Pt atoms from a convex surface with step sites is 379 keV [16], well above the incident electron energy of 200 keV. We therefore do not expect sputtering of atoms from the surface, only surface diffusion [63]. Next, dynamic structural changes are determined from the time series analysis using a hidden Markov model, of which the results are shown schematically in Fig. 3. The counting results for all frames are shown in Fig. S2 of the Supplemental Material [55].

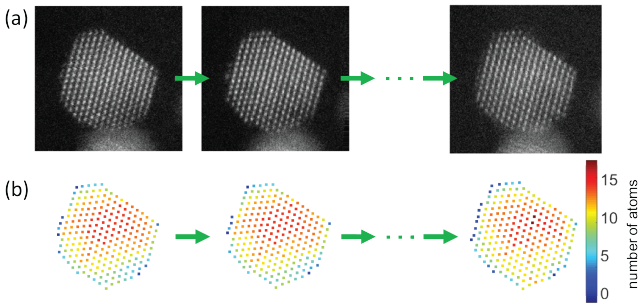

Figure 3. (a) The experimental ADF STEM time series of a Pt nanoparticle. (b) From the estimated hidden Markov model, the hidden state sequence is retrieved.

The HAADF STEM projection images reveal the faceted shape of the Pt nanoparticle. The {111} facets, on occasion decorated by additional atoms [66], are indicated by green crosses in Fig. 4(a). Using the counting results from our hidden Markov model analysis, we can now quantify the evolution of the number of atoms in these facets for each frame of the time series [Fig. 4(b)]. While the total number of atoms in the Pt nanoparticle remains the same, the number of atoms in the {111} facets along the beam direction decreases and the Pt nanoparticle gradually loses its faceted morphology during electron beam irradiation. This result is consistent with earlier observations of the same type of Pt nanoparticles [44] and can be explained by beam-induced surface diffusion. The hidden Markov model analysis has the added advantage that it enables us to quantify the probability for surface diffusion. From the transition probabilities shown in Fig. 4(c) it follows that the average probability for a surface atom to move to another column equals 4.6%. Taking into account the electron dose [63, 67], an experimental value for the average cross section for surface diffusion $\hat{\sigma} = 3.3 \times 10^{-6}$ Å^2, can even be determined. This cross section for surface diffusion includes the contributions of different migration mechanisms, such as hopping, atomic exchange, and vacancy diffusion, and from different types of surfaces [68, 69]. This value is of great importance in order to unravel dominant mechanisms and surfaces in the diffusion process and to gain new insights in surface related phenomena such as catalysis and nanoparticle growth.

In conclusion, we present a new statistical framework to reliably count the number of atoms in the atomic columns of a pure-element nanostructure in each frame of an ADF STEM time series using the so-called factorial hidden Markov model. As a proof of concept, we show that the performance of this new method significantly

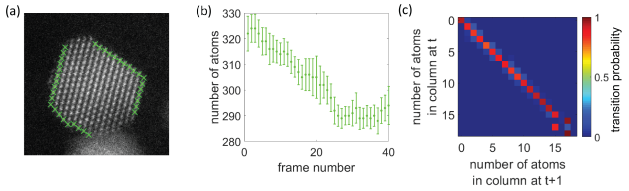

Figure 4. (a) The Pt nanoparticle shows clear facets along the beam direction. Atomic columns in {111} facets are indicated. (b) Number of atoms in the {111} facets indicated in (a). (c) Estimated transition probability matrix.

surpasses that of the current method for atom counting. This improved performance could be achieved since the hidden Markov model explicitly models the dynamics of the system. The new method is applied to an experimental time series of ADF STEM images of a catalyst Pt nanoparticle, and reveals the loss of the Pt nanoparticle's faceted morphology during the time series, due to the electron beam irradiation. Furthermore, our novel analysis approach enables us to quantify the probability and cross section for surface diffusion from a time-series of experimental ADF STEM images. The hidden Markov model for atom counting therefore holds promise for a reliable quantification of dynamic structural changes by adatom dynamics, surface diffusion, beam effects, or during *in situ* experiments. The hidden Markov model was implemented in the freely available StatSTEM software [2].

This project has received funding from the European Research Council (ERC) under the European Union's Horizon 2020 research and innovation programme (Grant Agreement No. 770887 and No. 823717 ESTEEM3). The authors acknowledge financial support from the Research Foundation Flanders (FWO, Belgium) through grants to A.D.w. and A.D.B. and projects G.0502.18N and EOS 30489208. L.J. acknowledges the SFI AMBER Centre for support. A.V. and P.D.N. acknowledge the UK Engineering and Physical Sciences Council (EPSRC) for support. A.V. also acknowledges Johnson-Matthey for support. We would like to thank Brian Theobald and Jonathan Sharman from JMTC Sonning for provision of the Pt sample.

† Present address: Johnson Matthey Technology Centre, Blounts Court Road, Sonning Common, Reading RG4 9NH, United Kingdom

* sandra.vanaert@uantwerpen.be

[1] P. L. Galindo, S. Kret, A. M. Sanchez, J.-Y. Laval, A. Yáñez, J. Pizarro, E. Guerrero, T. Ben, and S. I. Molina, The Peak Pairs algorithm for strain mapping from HRTEM images, Ultramicroscopy **107**, 1186 (2007).

[2] A. De Backer, K. H. W. van den Bos, W. Van den Broek, J. Sijbers, and S. Van Aert, StatSTEM: An efficient approach for accurate and precise model-based quantification of atomic resolution electron microscopy images, Ultramicroscopy **171**, 104 (2016).

[3] Y. Wang, U. Salzberger, W. Sigle, E. Suyolcu, and P. van Aken, Oxygen octahedra picker: A software tool to extract quantitative information from STEM images, Ultramicroscopy **168**, 46 (2016).

[4] M. Nord, P. E. Vullum, I. MacLaren, T. Tybell, and R. Holmestad, Atomap: a new software tool for automated analysis of atomic resolution images using two-dimensional Gaussian fitting, Adv. Struct. Chem. Imaging **3**, 9 (2017).

[5] J. Madsen, P. Liu, J. Kling, J. B. Wagner, T. W. Hansen, O. Winther, and J. Schiøtz, A Deep Learning Approach to Identify Local Structures in Atomic-Resolution Transmission Electron Microscopy Images, Advanced Theory and Simulations **1**, 1800037 (2018).

[6] F. e. a. de la Peña, hyperspy/hyperspy: Hyperspy v1.5.2 (2019).

[7] H. Chang, M. Saito, T. Nagai, Y. Liang, Y. Kawazoe, Z. Wang, H. Wu, K. Kimoto, and Y. Ikuhara, Single adatom dynamics at monatomic steps of free-standing few-layer reduced graphene, Sci. Rep. **4**, 6037 (2015).

[8] T. Furnival, D. Knez, E. Schmidt, R. K. Leary, G. Kothleitner, F. Hofer, P. D. Bristowe, and P. A. Midgley, Adatom dynamics and the surface reconstruction of Si(110) revealed using time-resolved electron microscopy, Appl. Physics Lett. **113**, 183104 (2018).

[9] A. Surrey, D. Pohl, L. Schultz, and B. Rellinghaus, Quantitative Measurement of the Surface Self-Diffusion on Au Nanoparticles by Aberration-Corrected Transmission Electron Microscopy, Nano Lett. **12**, 6071 (2012).

[10] S. Schneider, A. Surrey, D. Pohl, L. Schultz, and B. Rellinghaus, Atomic surface diffusion on Pt nanoparticles quantified by high-resolution transmission electron microscopy, Micron **63**, 52 (2014).

[11] V. Cherepanov and B. Voigtländer, Influence of material, surface reconstruction, and strain on diffusion at the Ge(111) surface, Phys. Rev. B **69**, 125331 (2004).

[12] P. A. Buffat, Electron diffraction and HRTEM studies of multiply-twinned structures and dynamical events in metal nanoparticles: facts and artefacts, Mater. Chem. Phys. **81**, 368 (2003).

[13] J. Yu, X. Li, J. Miao, W. Yuan, S. Zhou, B. Zhu, Y. Gao, H. Yang, Z. Zhang, and Y. Wang, Atomic Mechanism in Layer-by-Layer Growth via Surface Reconstruction, Nano Lett. **19**, 4205 (2019).

[14] S. Iijima and T. Ichihashi, Structural Instability of Ultrafine Particles of Metals, Phys. Rev. Lett. **56**, 616 (1986).

[15] P. E. Batson, Motion of Gold Atoms on Carbon in the Aberration-Corrected STEM, Microsc. Microanal. **14**, 89 (2008).

[16] R. F. Egerton, R. McLeod, F. Wang, and M. Malac, Basic questions related to electron-induced sputtering in the TEM, Ultramicroscopy **110**, 991 (2010).

[17] J. Lee, W. Zhou, J. Pennycook, J.-C. Idrobo, and S. T. Pantelides, Direct visualization of reversible dynamics in a Si6 cluster embedded in a graphene pore, Nat. Commun. **4**, 1650 (2013).

[18] M. L. Taheri, E. A. Stach, I. Arslan, P. A. Crozier, B. C. Kabius, T. LaGrange, A. M. Minor, S. Takeda, M. Tanase, J. B. Wagner, and R. Sharma, Current status and future directions for in situ transmission electron microscopy, Ultramicroscopy **170**, 86 (2016).

[19] T. Altantzis, I. Lobato, A. De Backer, A. Béché, Y. Zhang, S. Basak, M. Porcu, Q. Xu, A. Sánchez-Iglesias, L. M. Liz-Marzán, G. Van Tendeloo, S. Van Aert, and S. Bals, Three-Dimensional Quantification of the Facet Evolution of Pt Nanoparticles in a Variable Gaseous Environment, Nano Lett. **19**, 477 (2019).

[20] M. R. Armstrong, K. Boyden, N. D. Browning, G. H. Campbell, J. D. Colvin, W. J. DeHope, A. M. Frank, D. J. Gibson, F. Hartemann, J. S. Kim, W. E. King, T. B. LaGrange, B. J. Pyke, B. W. Reed, R. M. Shuttlesworth, B. C. Stuart, and B. R. Torralva, Practical considerations for high spatial and temporal resolution dynamic transmission electron microscopy, Ultramicroscopy **107**, 356 (2007).

[21] N. D. Browning, M. A. Bonds, G. H. Campbell, J. E. Evans, T. LaGrange, K. L. Jungjohann, D. J. Masiel, J. McKeown, S. Mehraeen, B. W. Reed, and M. Santala, Recent developments in dynamic transmission electron microscopy, Curr. Opin. Solid State Mater. Sci. **16**, 23 (2012).

[22] B. Barwick, H. S. Park, O.-H. Kwon, and A. H. Baskin, J. S. Zewail, 4D Imaging of Transient Structures and Morphologies in Ultrafast Electron Microscopy, Science **322**, 1227 (2008).

[23] B. J. Siwick, J. R. Dwyer, R. E. Jordan, and R. J. D. Miller, An Atomic-Level View of Melting Using Femtosecond Electron Diffraction, Science **302**, 1382 (2003).

[24] A. H. Zewail, 4D Ultrafast Electron Diffraction, Crystallography, and Microscopy, Annu. Rev. Phys. Chem. **57**, 65 (2006).

[25] C.-Y. Ruan, Y. Murooka, R. K. Raman, and R. A. Murdick, Dynamics of Size-Selected Gold Nanoparticles Studied by Ultrafast Electron Nanocrystallography, Nano Lett. **7**, 1290 (2007).

[26] C.-Y. Ruan, Y. Murooka, R. K. Raman, and R. A. Murdick, The Development and Applications of Ultrafast Electron Nanocrystallography, Microsc. Microanal. **15**, 323 (2009).

[27] A. A. Ischenko and S. A. Aseyev, Chapter Three - Ultrafast Electron Crystallography and Nanocrystallography, in *Time-Resolved Electron Diffraction*, Advances in Imaging and Electron Physics, Vol. 184, edited by A. A. Ischenko and S. A. Aseyev (Elsevier, 2014) pp. 101 – 143.

[28] C. Rischel, A. Rousse, I. Uschmann, P.-A. Albouy, J.-P. Geindre, P. Audebert, J.-C. Gauthier, E. Förster, J.-L. Martin, and A. Antonetti, Femtosecond time-resolved X-ray diffreaction from laser-heated organic films, Nature (London) **390**, 490 (1997).

[29] A. M. Lindenberg, S. L. Johnson, and D. A. Reis, Visualization of Atomic-Scale Motions in Materials via Femtosecond X-Ray Scattering Techniques, Annu. Rev. Mater. Res. **47**, 425 (2017).

[30] C. L. Jia, S. B. Mi, J. Barthel, D. W. Wang, R. E. Dunin-Borkowski, K. W. Urban, and A. Thust, Determination of the 3D shape of a nanoscale crystal with atomic resolution from a single image, Nat. Mater. **13**, 1044 (2014).

[31] M. Linck, B. Freitag, S. Kujawa, M. Lehmann, and T. Niermann, State of the art in atomic resolution off-axis electron holography, Ultramicroscopy **116**, 13 (2012).

[32] S. Van Aert, K. J. Batenburg, M. D. Rossell, R. Erni, and G. Van Tendeloo, Three-dimensional atomic imaging of crystalline nanoparticles, Nature (London) **470**, 374 (2011).

[33] S. Van Aert, A. De Backer, G. T. Martinez, B. Goris, S. Bals, G. Van Tendeloo, and A. Rosenauer, Procedure to count atoms with trustworthy single-atom sensitivity, Phys. Rev. B **87**, 064107 (2013).

[34] M. Isaacson, D. Kopf, M. Utlaut, N. W. Parker, and A. V. Crewe, Direct observations of atomic diffusion by scanning transmission electron microscopy, Proc. Natl. Acad. Sci. U.S.A. **74**, 1802 (1977).

[35] H.-G. Liao, D. Zherebetskyy, H. Xin, C. Czarnik, P. Ercius, H. Elmlund, M. Pan, L.-W. Wang, and H. Zheng, Facet development during platinum nanocube growth, Science **345**, 916 (2014).

[36] J. Kotakoski, C. Mangler, and J. C. Meyer, Imaging atomic-level random walk of a point defect in graphene, Nat. Commun. **5**, 3991 (2014).

[37] R. Mishra, R. Ishikawa, A. R. Lupini, and S. J. Pennycook, Single-atom dynamics in scanning transmission electron microscopy, MRS Bull. **42**, 644 (2017).

[38] P. Liu, T. Wu, J. Madsen, J. Schiøtz, J. B. Wagner, and T. W. Hansen, Transformations fo supported gold nanoparticles observed by in situ electron microscopy, Nanoscale **11**, 11885 (2019).

[39] J. Zhou, Y. Yang, Y. Yang, D. S. Kim, A. Yuan, X. Tian, C. Ophus, F. Sun, A. K. Schmid, M. Nathanson, H. Heinz, Q. An, H. Zeng, P. Ercius, and J. Miao, Observing crystal nucleation in four dimensions using atomic electron tomography, Nature (London) **570**, 500 (2019).

[40] S. Van Aert, J. Verbeeck, R. Erni, S. Bals, M. Luysberg, D. Van Dyck, and G. Van Tendeloo, Quantitative atomic resolution mapping using high-angle annular dark field scanning transmission electron microscopy, Ultramicroscopy **109**, 1236 (2009).

[41] H. E, K. E. MacArthur, T. J. Pennycook, E. Okunishi, A. J. D'Alfonso, N. R. Lugg, L. J. Allen, and P. D. Nellist, Probe integrated scattering cross sections in the analysis of atomic resolution HAADF STEM images, Ultramicroscopy **133**, 109 (2013).

[42] A. De Backer, A. De wael, J. Gonnissen, and S. Van Aert, Optimal experimental design for nano-particle atom-counting from high-resolution STEM images, Ultramicroscopy **151**, 46 (2015).

[43] J. M. LeBeau, S. D. Findlay, L. J. Allen, and S. Stemmer, Standardless atom counting in scanning transmission electron microscopy, Nano Lett. **10**, 4405 (2010).

[44] L. Jones, K. E. MacArthur, V. T. Fauske, A. T. J. van Helvoort, and P. D. Nellist, Rapid estimation of catalyst nanoparticle morphology and atomic-coordination by high-resolution Z-contrast electron microscopy, Nano Lett. **14**, 6336 (2014).

[45] A. De Backer, G. T. Martinez, A. Rosenauer, and S. Van Aert, Atom counting in HAADF STEM using a statistical model-based approach: Methodology, possibilities, and inherent limitations, Ultramicroscopy **134**, 23 (2013).

[46] A. De wael, A. De Backer, L. Jones, P. D. Nellist, and S. Van Aert, Hybrid statistics-simulations based method for atom-counting using scanning transmission electron microscopy, Ultramicroscopy **177**, 69 (2017).

[47] S. Bals, S. Van Aert, C. P. Romero, K. Lauwaet, M. J. Van Bael, B. Schoeters, B. Partoens, E. Yücelen, P. Lievens, and G. Van Tendeloo, Atomic scale dynamics of ultrasmall germanium clusters, Nat. Commun. **3**, 897 (2012).

[48] J. J. Geuchies, C. van Overbeek, W. H. Evers, B. Goris,

A. De Backer, G. P. Gantapara, F. T. Rabouw, J. Hilhorst, J. L. Peters, O. Konovalov, A. V. Petukhov, M. Dijkstra, L. D. A. Siebbeles, S. Van Aert, S. Bals, and D. Vanmaekelbergh, In situ study of the formation mechanism of two-dimensional superlattices from PbSe nanocrystals, Nat. Mater. **15**, 1248 (2016).

[49] A. De Backer, L. Jones, I. Lobato, T. Altantzis, B. Goris, P. D. Nellist, S. Bals, and S. Van Aert, Three-dimensional atomic models from a single projection using Z-contrast imaging: verification by electron tomography and opportunities, Nanoscale **9**, 8791 (2017).

[50] L. R. Rabiner, A tutorial on hidden Markov models and selected applications in speech recognition, Proceedings of the IEEE **77**, 257 (1989).

[51] J. A. Bilmes, A Gentle Tutorial of the EM Algorithm and its Application to Parameter Estimation for Gaussian Mixture and Hidden Markov Models, International Computer Science Institute Berkeley **TR-97-021** (1998).

[52] S. R. Eddy, What is a hidden Markov model?, Nat. Biotechnol. **22**, 1315 (2004).

[53] C. Bishop, *Pattern Recognition and Machine Learning* (Springer-Verlag, New York, 2006).

[54] P. Dymarski, *Hidden Markov Models, Theory and Applications* (InTech, 2011).

[55] See Supplemental Material for technical details on algorithms, simulation and experimental set-up, and all images of the experimental time series of the Pt nanoparticle, .

[56] Z. Ghahramani and M. I. Jordan, Factorial Hidden Markov Models, Mach. Learn. **29**, 245 (1997).

[57] K. E. MacArthur, A. J. D'Alfonso, D. Ozkaya, L. Allen, and P. Nellist, Optimal ADF STEM imaging parameters for tilt-robust image quantification, Ultramicroscopy **156**, 1 (2015).

[58] G. McLachlan and D. Peel, Finite Mixture Models (Wiley Series in Probability and Statistics. John Wiley and Sons, Inc., 2000).

[59] A. J. Viterbi, Error bounds for convolutional codes and an asymptotically optimum decoding algorithm, IEEE Trans. Inf. Theory **13**, 260 (1967).

[60] G. D. Forney, The Viterbi algorithm, IEEE Trans. Inf. Theory **61**, 268 (1973).

[61] A. De Backer, G. T. Martinez, K. E. MacArthur, L. Jones, A. Béché, P. D. Nellist, and S. Van Aert, Dose limited reliability of quantitative annular dark field scanning transmission electron microscopy for nano-particle atom-counting, Ultramicroscopy **151**, 56 (2015).

[62] A. M. Varambhia, L. Jones, A. De Backer, V. T. Fauske, S. Van Aert, D. Ozkaya, and P. D. Nellist, Quantifying a Heterogeneous Ru Catalyst on Carbon Black Using ADF STEM, Part. Part. Syst. Charact. **33**, 438 (2016).

[63] S. Van Aert, A. De Backer, L. Jones, G. T. Martinez, A. Béché, and P. D. Nellist, Control of Knock-On Damage for 3D Atomic Scale Quantification of Nanostructures: Making Every Electron Count in Scanning Transmission Electron Microscopy, Phys. Rev. Lett. **122**, 066101 (2019).

[64] L. Jones, H. Yang, T. J. Pennycook, M. S. J. Marshall, S. Van Aert, N. D. Browning, M. R. Castell, and P. D. Nellist, Smart Align - a new tool for robust non-rigid registration of scanning microscope data, Adv. Struct. Chem. Imaging **1**, 8 (2015).

[65] J. Fatermans, A. J. den Dekker, K. Müller-Caspary, I. Lobato, C. M. O'Leary, P. D. Nellist, and S. Van Aert, Single Atom Detection from Low Contrast-to-Noise Ratio Electron Microscopy Images, Phys. Rev. Lett. **121**, 056101 (2018).

[66] Z. W. Wang and R. E. Palmer, Mass Spectrometry and Dynamics of Gold Adatoms Observed on the Surface of Size-Selected Au Nanoclusters, Nano Lett. **12**, 91 (2012).

[67] R. F. Egerton, Beam-Induced Motion of Adatoms in the Transmission Electron Microscope, Microsc. Microanal. **19**, 479 (2013).

[68] K. Oura, M. Katayama, A. V. Zotov, V. G. Lifshits, and A. A. Saranin, Elementary Processes at Surfaces II. Surface Diffusion, in *Surface Science - An Introduction* (Springer Berlin Heidelberg, Berlin, Heidelberg, 2003) Chap. 13, pp. 325–356.

[69] R. F. Egerton, Radiation damage to organic and inorganic specimens in the TEM, Micron **119**, 72 (2019).

Supplementary Material
Measuring dynamic structural changes of nanoparticles at the atomic scale using electron microscopy

Annelies De wael,[1,2] Annick De Backer,[1,2] Lewys Jones,[3,4,5]
Aakash Varambhia,[3,†] Peter D. Nellist,[3] and Sandra Van Aert[1,2,*]

[1] *EMAT, University of Antwerp, Groenenborgerlaan 171, 2020 Antwerp, Belgium*
[2] *NANOlab Center of Excellence, University of Antwerp, Belgium*
[3] *Department of Materials, University of Oxford, Parks Road, OX1 3PH Oxford, United Kingdom*
[4] *Advanced Microscopy Laboratory, Centre for Research on Adaptive Nanostructures and Nanodevices (CRANN), Dublin 2, Ireland*
[5] *School of Physics, Trinity College Dublin, The University of Dublin, Dublin 2, Ireland*

1. PARAMETER ESTIMATION

Table I summarizes the notation used for the factorial hidden Markov model for atom counting.

1.1. Expectation-Maximisation algorithm

The expectation-maximisation algorithm for the factorial hidden Markov model for atom counting, also called the Baum-Welch algorithm, updates the parameter estimates in order to maximize the complete data likelihood expressed by equations (1)-(4) [1].

$$\begin{aligned} &p(\mathbf{H},\mathbf{O};\boldsymbol{\Omega}) \\ &= p\left(\mathbf{h}_1;\mathbf{I}\right)\prod_{t=2}^{T} p\left(\mathbf{h}_t|\mathbf{h}_{t-1};\mathbf{A}\right)\prod_{t'=1}^{T} p\left(\mathbf{o}_{t'}|\mathbf{h}_{t'};\boldsymbol{\mu},\sigma\right), \end{aligned} \quad (1)$$

with

$$p\left(\mathbf{h}_1;\mathbf{I}\right) = \prod_{n=1}^{N}\prod_{g=0}^{G} \iota_g^{h_{1g}^{(n)}}, \quad (2)$$

$$p\left(\mathbf{h}_t|\mathbf{h}_{t-1};\mathbf{A}\right) = \prod_{n=1}^{N}\prod_{g_1=0}^{G}\prod_{g_2=0}^{G} A_{g_1 g_2}^{h_{t-1,g_1}^{(n)} h_{t,g_2}^{(n)}}, \quad (3)$$

$$p\left(\mathbf{o}_t|\mathbf{h}_t;\boldsymbol{\mu},\sigma\right) = \prod_{n=1}^{N}\prod_{g=0}^{G} \mathcal{N}\left(o_t^{(n)}|\mu_g,\sigma\right)^{h_{tg}^{(n)}}, \quad (4)$$

where $\mu_g = a\mathcal{M}_g$, with a a linear scaling parameter and $\mathcal{M}_g$ the simulated scattering cross section for a column with g atoms (also called library value).

In the M-step, the parameters are updated to maximize the likelihood, using the following update formulas:

$$\iota_g = \frac{\sum_{n=1}^{N}\mathbb{E}\left[h_{1g}^{(n)}\right]}{\sum_{n=1}^{N}\sum_{j=0}^{G}\mathbb{E}\left[h_{1j}^{(n)}\right]}, \quad (5)$$

$$A_{jg} = \frac{\sum_{t=2}^{T}\sum_{n=1}^{N}\mathbb{E}\left[h_{tg}^{(n)}h_{t-1,j}^{(n)}\right]}{\sum_{t=2}^{T}\sum_{n=1}^{N}\sum_{g'=0}^{G}\mathbb{E}\left[h_{tg'}^{(n)}h_{t-1,j}^{(n)}\right]}, \quad (6)$$

$$a = \frac{\sum_{t=1}^{T}\sum_{n=1}^{N}\sum_{g=0}^{G}\mathbb{E}\left[h_{tg}^{(n)}\right]\mathbf{o}_t^{(n)}\mathcal{M}_g}{\sum_{t=1}^{T}\sum_{n=1}^{N}\sum_{g=0}^{G}\mathbb{E}\left[h_{tg}^{(n)}\right]\mathcal{M}_g^2}, \quad (7)$$

$$\sigma = \sqrt{\frac{\sum_{t=1}^{T}\sum_{n=1}^{N}\sum_{g=0}^{G}\mathbb{E}\left[h_{tg}^{(n)}\right](\mathbf{o}_t^{(n)} - a\mathcal{M}_g)^2}{\sum_{t=1}^{T}\sum_{n=1}^{N}\sum_{g=0}^{G}\mathbb{E}\left[h_{tg}^{(n)}\right]}}. \quad (8)$$

During the E-step of the algorithm, the quantities $\mathbb{E}\left[h_{tg}^{(n)}\right]$ and $\mathbb{E}\left[h_{tg}^{(n)}h_{t-1,j}^{(n)}\right]$ are determined, and the likelihood is calculated. The iterative algorithm keeps updating the parameter estimates until the value of the likelihood has converged. As such we obtain maximum likelihood estimates of the model parameters of the factorial hidden Markov model for atom counting.

1.2. Viterbi algorithm

Next, the hidden state sequence is retrieved based on the estimated parameters using a path backtracking algorithm, called the Viterbi algorithm [2, 3]. The goal of the Viterbi algorithm for hidden Markov models is to determine the most likely hidden state sequence. We could determine the individually most likely state of column n at time t, $\mathbf{h}_t^{(n)}$, as the state that maximizes the $\mathbb{E}\left[h_{tg}^{(n)}\right]$, but the transition probability from $t-1$ to this state at time t may be zero, causing this state to be invalid. Therefore, the Viterbi algorithm considers the

† Present address: Johnson Matthey Technology Centre, Blounts Court Road, Sonning Common, Reading RG4 9NH, United Kingdom
* sandra.vanaert@uantwerpen.be

Symbol	Explanation
T	Number of frames in the time series
N	Number of atomic columns in each frame
G	Maximum number of atoms in a column during the time series
$\mathbf{H}$	$T \times N \times (G+1)$ tensor with hidden states: $\mathbf{H} = \{\mathbf{h}_t\}$
$\mathbf{h}_t$	$N \times (G+1)$ binary state matrix at time t: $\mathbf{h}_t = \left\{h_{tg}^{(n)}\right\}$
$h_{tg}^{(n)}$	Binary state variable: $h_{tg}^{(n)} = 1$ if column n has g atoms at time t
$\mathbf{O}$	$T \times N$ matrix with observed states: $\mathbf{O} = \{\mathbf{o}_t\}$
$\mathbf{o}_t$	$1 \times N$ observed vector at time t: $\mathbf{o}_t = \left\{o_t^{(n)}\right\}$
$o_t^{(n)}$	Scattering cross section of column n at time t
$\mathbf{I}$	$(G+1) \times 1$ initial probability vector: $\mathbf{I} = \{\iota_g\}$
ι_g	Initial probability for a column to have g atoms in frame 1
$\mathbf{A}$	$(G+1) \times (G+1)$ transition matrix: $\mathbf{A} = \{A_{jg}\}$
A_{jg}	Transition probability from j to g atoms between two frames
$\boldsymbol{\mu}$	$G \times 1$ vector with elements μ_g
μ_g	Average scattering cross section corresponding to g atoms in a column
$\mathcal{M}_g$	Library value for a column with g atoms
a	Scaling parameter relating the average scattering cross section to the library: $\mu_g = a\mathcal{M}_g$
σ	Width of the Gaussian distribution around the average scattering cross section

Table I: Notation overview

entire state sequence.

In the following, we will write the actual number of atoms in column n at time t as $q_t^{(n)}$. This quantity equals the number of atoms $q_t^{(n)} = g$ for which the previously introduced binary state variable $h_{tg}^{(n)} = 1$. In order to retrieve the realized state sequence, given the observations, we define the following quantity:

$$\delta(t,n,g) = \max_{q_1^{(n)},\cdots,q_{t-1}^{(n)}} \left[P\left(q_1^{(n)} \cdots q_t^{(n)} = g, o_1^{(n)} \cdots o_t^{(n)}\right)\right]. \tag{9}$$

This expresses the score, i.e. the highest probability, along a single path, at time t for column n, which accounts for the first t observations of that column, and ends with g atoms in column n at time t. In the next frame, $t+1$, we obtain the score by induction:

$$\delta(t+1,n,g) = \max_{0\le j\le G} \left[\delta(t,n,j)A_{jg}\right] \cdot \mathcal{N}\left(o_{t+1}^{(n)}|\mu_g,\sigma\right). \tag{10}$$

This expression leads to the complete data likelihood from equation (1) at time T:

$$P(\mathbf{H}=\mathbf{Q},\mathbf{O}) = \prod_{n=1}^{N}\left(\max_{0\le g\le G}\left[\delta(T,n,g)\right]\right), \tag{11}$$

with the hidden state sequence $\mathbf{H}$ equal to the most likely path $\mathbf{Q}$ retrieved by the Viterbi algorithm.

The algorithm calculates the score δ and keeps track of the number of atoms that maximizes this probability in an argument array ϕ. First, these quantities are initialized as follows:

$$\delta(1,n,g) = \iota_g \mathcal{N}\left(o_1^{(n)}|\mu_g,\sigma\right), \tag{12}$$

$$\phi(1,n,g) = 0, \tag{13}$$

with $\delta(1,n,g)$ the score for state g in column n at time t and ϕ the argument array.

The state with the best score for column n at a time t, is used to determine the scores for all possible states of that column n at the next time $t+1$, expressed by

$$\delta(t+1,n,g) = \max_{0\le j\le G}\left[\delta(t,n,j)A_{jg}\right] \cdot \mathcal{N}\left(o_{t+1}^{(n)}|\mu_g,\sigma\right), \tag{14}$$

$$\phi(t+1,n,g) = \arg\max_{0\le j\le G}\left[\delta(t,n,j)A_{jg}\right], \tag{15}$$

where the number of atoms maximising the score is saved in the argument array.

In the final image of the time series, at time T, the number of atoms that maximizes the score for column n is equal to:

$$q_T^{(n)} = \arg\max_{0\le g\le G}\left[\delta(T,n,g)\right]. \tag{16}$$

Finally, by path backtracking, the most likely hidden state sequence is retrieved:

$$q_t^{(n)} = \phi\left(t+1,n,q_{t+1}^{(n)}\right), \tag{17}$$

yielding the the number of atoms in each column at each time.

2. DETAILS FOR THE SIMULATIONS OF THE HYPOTHETIC ADF STEM SERIES

We simulated scattering cross sections corresponding to hypothetic ADF STEM time series with 40 frames of a changing Pt nanoparticle with 215 atomic columns, and a thickness up to 15 atoms. The number of atoms in a column was allowed to change by ± 1 from frame to frame throughout the time series, with a probability of 10%. The scattering cross sections of each atomic column are generated from a Pt library, using Poisson random draws in order to replicate the uncertainty from the finite electron dose. Additionally, scan distortion is included in the simulation of the scattering cross sections. Based on a previous study, the effect of scan distortion has been modeled as a normal distribution, with an experimentally determined variance of $4.5 \cdot 10^{-4} \mu_g$, with μ_g the average scattering cross section of an atomic column with g atoms [4]. For each electron dose, 200 different noise realizations of such time series were constructed. Using these data, we compare the atom counts obtained by the hidden Markov model and the collective hybrid method with the ground truth.

3. PT TIME SERIES

In Fig. S1, we show all frames of the time series of the catalyst Pt nanoparticle analyzed in this paper, after image registration. From this series we can see that small amounts of sample tilt are present in some of the images. Furthermore, we see that the particle remains stable during acquisition. The counting results obtained by the hidden Markov model of the tilt-compensated time series are shown in Fig. S2. The experimental time series and corresponding counting results are also shown in the Supplementary Animations.

[1] L. R. Rabiner, "A tutorial on hidden Markov models and selected applications in speech recognition," Proceedings of the IEEE **77**, 257–286 (1989).

[2] A. J. Viterbi, "Error bounds for convolutional codes and an asymptotically optimum decoding algorithm," IEEE Transactions on Information Theory **13**, 260–269 (1967).

[3] G. D. Forney, "The Viterbi algorithm," IEEE Transactions on Information Theory **61**, 268–278 (1973).

[4] S. Van Aert, A. De Backer, L. Jones, G. T. Martinez, A. Béché, and P. D. Nellist, "Control of Knock-On Damage for 3D Atomic Scale Quantification of Nanostructures: Making Every Electron Count in Scanning Transmission Electron Microscopy," Physical Review Letters **122**, 066101 (2019).

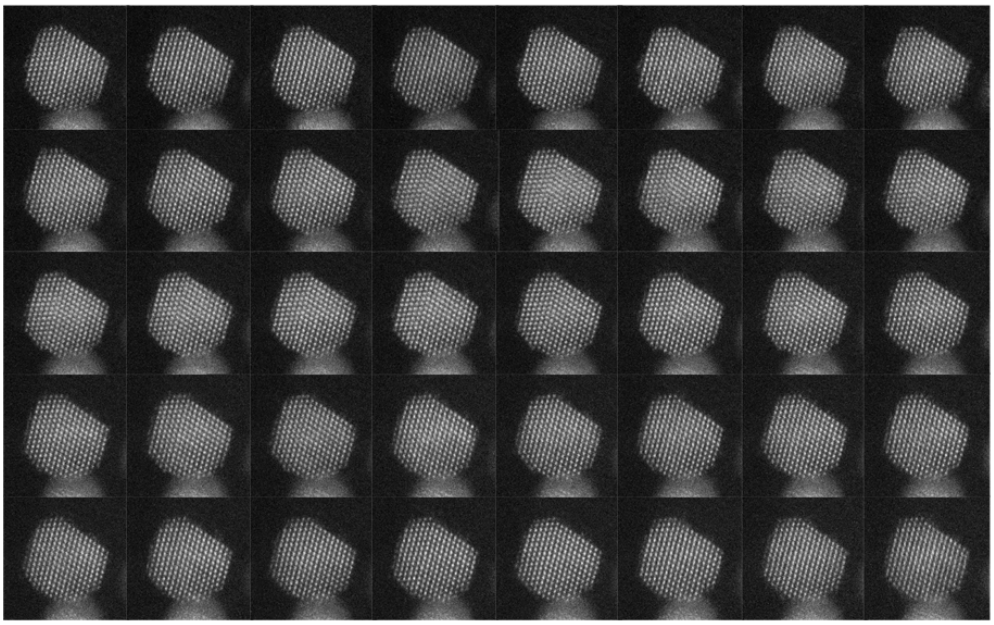

Figure S1: Experimental ADF STEM time series recorded of a Pt nanoparticle. Time progresses along the rows.

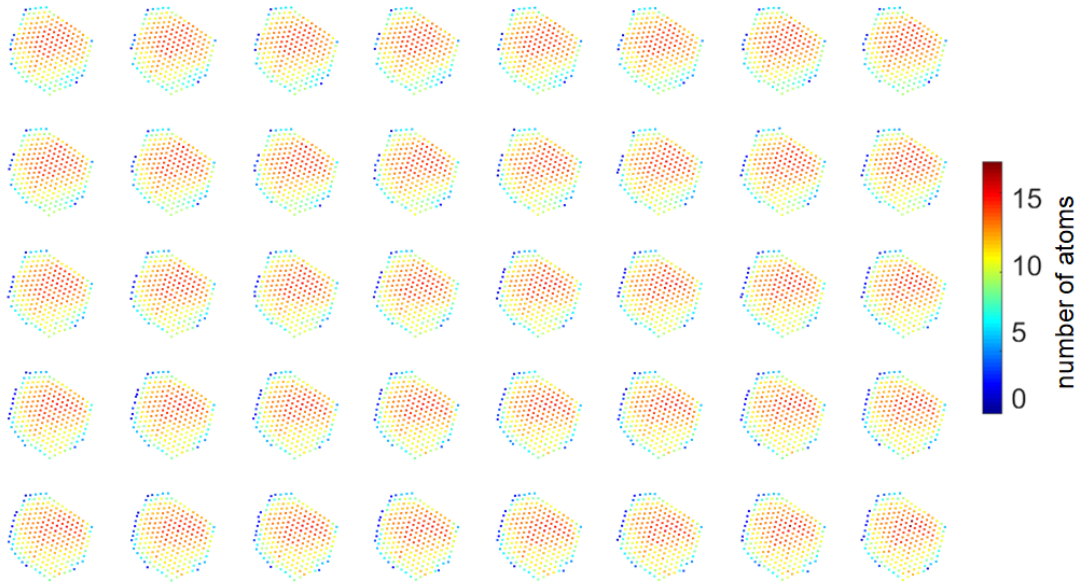

Figure S2: Counting results obtained by the hidden Markov model for the time series from Fig. S1.